ADVANCES IN ATMOSPHERIC SCIENCES, VOL. 39, JULY 2022, 1133–1150

• **Original Paper** •

# Change in Precipitation over the Tibetan Plateau Projected by Weighted CMIP6 Models※

Yin ZHAO[1,3], Tianjun ZHOU[*1,2], Wenxia ZHANG[1], and Jian LI[3]

[1]*LASG, Institute of Atmospheric Physics, Chinese Academy of Science, Beijing* 100029, *China*
[2]*University of Chinese Academy of Sciences, Beijing* 100049, *China*
[3]*State Key Laboratory of Severe Weather, Chinese Academy of Meteorological Sciences, China Meteorological Administration, Beijing* 100049, *China*

(Received 27 October 2021; revised 22 February 2022; accepted 25 March 2022)

ABSTRACT

Precipitation over the Tibetan Plateau (TP) is important to local and downstream ecosystems. Based on a weighting method considering model skill and independence, changes in the TP precipitation for near-term (2021–40), mid-term (2041–60) and long-term (2081–2100) under shared socio-economic pathways (SSP1-1.9, SSP1-2.6, SSP2-4.5, SSSP3-7.0, SSP5-8.5) are projected with 27 models from the latest Sixth Phase of the Couple Model Intercomparison Project. The annual mean precipitation is projected to increase by 7.4%–21.6% under five SSPs with a stronger change in the northern TP by the end of the 21st century relative to the present climatology. Changes in the TP precipitation at seasonal scales show a similar moistening trend to that of annual mean precipitation, except for the drying trend in winter precipitation along the southern edges of the TP.

Weighting generally suggests a slightly stronger increase in TP precipitation with reduced model uncertainty compared to equally-weighted projections. The effect of weighting exhibits spatial and seasonal differences. Seasonally, weighting leads to a prevailing enhancement of increase in spring precipitation over the TP. Spatially, the influence of weighting is more remarkable over the northwestern TP regarding the annual, summer and autumn precipitation. Differences between weighted and original MMEs can give us more confidence in a stronger increase in precipitation over the TP, especially for the season of spring and the region of the northwestern TP, which requires additional attention in decision making.

**Key words:** model weighting, precipitation, the Tibetan Plateau, CMIP6, projection

**Citation:** Zhao, Y., T. J. Zhou, W. X. Zhang, and J. Li, 2022: Change in precipitation over the Tibetan Plateau projected by weighted CMIP6 models. *Adv. Atmos. Sci.*, **39**(7), 1133−1150, https://doi.org/10.1007/s00376-022-1401-2.

**Article Highlights:**

- The annual mean precipitation over the TP will increase with a relatively greater change in the north regarding the long-term projection.
- Changes in the TP precipitation at seasonal scales show a similar moistening trend to that of annual mean precipitation, except for winter.
- Weighting suggests a slightly greater increase in TP precipitation and reduced model uncertainty, with spatial and seasonal differences.
- Weighting implies greater increase in TP precipitation than raw projections, especially for spring and the northwestern TP.

## 1. Introduction

The TP is known as the Asian water tower, as the precipitation and glaciers there nourish more than 10 major Asian rivers (Immerzeel et al., 2010; Immerzeel and Bierkens, 2012). The TP precipitation has influence on large-scale circulations, like the Western Pacific subtropical high and the East Asian summer monsoon, through modulating the heat source over the TP (Duan et al., 2017; Liu et al., 2020). It is observed that the precipitation over the TP has decreased over the southeastern TP and increased over the northwestern TP since 1979, which contributes to the melting (advancing) of glaciers over the southeastern (northwestern) TP in

※ This paper is a contribution to the special issue on Third Pole Atmospheric Physics, Chemistry, and Hydrology.

* Corresponding author: Tianjun ZHOU
Email: zhoutj@lasg.iap.ac.cn

addition to the warming climate (Yao et al., 2012). In view of the importance of the TP precipitation to the local and downstream ecosystems, it is crucial to know the changes in TP precipitation under global warming, which has far-reaching influences on the climate system and water management in the related Asian countries for the future (Pritchard, 2019; Immerzeel et al., 2020).

Simulated by GCMs, the precipitation over the TP is projected to increase with the radiation forcing, as a response to the enhanced evaporation and upward water vapor transport (Hao et al., 2013; Su et al., 2013; Hu et al., 2015; Zhang et al., 2015; Feng and Zhou, 2017; Li et al., 2021; Xie and Wang, 2021; Yang et al., 2021). In regional or downscaling simulations, the precipitation over the southern TP is projected to decrease in summer, which is related to the dynamic process reproduced by regional models with higher resolution (Ji and Kang, 2013; Wang et al., 2018; Zhang et al., 2019; Zhang and Gao, 2020; Fu et al., 2021). In addition, the extreme precipitation over the TP is also projected to increase, including the precipitation intensity and frequency (Gao et al., 2018; Zhou et al., 2020; Li et al., 2021). Although great efforts have been made, the picture of future changes in precipitation over the TP is still clouded by the uncertainty of these projections. For instance, projections by GCMs show a large envelope as a result from different climate sensitivities and scenarios considered. In addition, changes in precipitation over the southern TP in summer differ between projections by GCMs and regional models. Zhou et al. (2020) estimated the ranges and uncertainties of projected precipitation over the TP and found the largest uncertainty is located at the western and northern edges of TP. Considering the currently limited knowledge of natural climate sensitivity and uncertain scenarios in the future, it is necessary to ensure a sample size of model simulations to embrace all the possibilities of future climate, while taking into account the different performances of models used (Xu et al., 2010).

To improve the projection of future climate and reduce the model uncertainty, a weighting method has been developed in recent years, which gives models different weights according to their skill and independence (Sanderson et al., 2015a, b, 2017; Brunner et al., 2020). This method has been applied to the projection of a range of variables, including global temperature, maximum temperature in North America, temperature and precipitation in Europe, total and extreme precipitation over China, Arctic sea ice and Antarctic ozone concentrations (Knutti et al., 2017; Lorenz et al., 2018; Brunner et al., 2019, 2020; Amos et al., 2020; Liang et al., 2020; Merrifield et al., 2020; Li et al., 2021). The weighting method shows potential for providing a more reasonable ensemble mean of models and reducing the uncertainty of projections (Brunner et al., 2020). For instance, the ensemble mean of 17 CMIP5 models based on performance and independence performs better than a rank-based weighting method and the simple arithmetic mean in reproducing total and extreme precipitation over China, especially for western China (Li et al., 2021). Given the large uncertainty in projecting TP precipitation (Zhou et al., 2020), whether the projection could be improved by the weighting method remains unknown.

With 27 models from the newly released CMIP6 (the Sixth Phase of the Couple Model Intercomparison Project; Eyring et al., 2016), we aim to address the following questions: (1) How will precipitation over the TP change by the end-of-century (2081–2100) relative to the historical period from 1985 to 2014 in the projection of the advanced CMIP6 models? (2) What is the impact of weighting the CMIP6 models with their skill and independence on the projection of the TP precipitation?

The remaining part of the paper is organized as follows. Data and the analysis methods used are introduced in section 2. Results are shown in section 3 and the conclusions are summarized in section 4.

## 2. Data and methods

### 2.1. *Model data*

The TP region in this study is defined as areas above 2500 m as shown in Fig. 1. Monthly precipitation data simulated by 27 models from CMIP6 is used in the study (Table 1). The basic information, including the modeling center, model acronym and horizontal resolution, is summarized in Table 1. More information about the CMIP6 models can be found at https://esgf-node.llnl.gov/search/cmip6/. The data is interpolated onto a 1° × 1° grid using bilinear interpolation. The historical and SSP1-1.9, SSP1-2.6, SSP2-4.5, SSSP3-7.0, SSP5-8.5 simulations from each model are used in the study. The scenarios are the combination of Shared Socioeconomic Pathways (SSP) and radiation forcing levels (O'Neill et al., 2016; Riahi et al., 2017). The period of 1985–2014 in the historical record is regarded as the present climatology. For future change, we focus on the period of 2021–40, 2041–60 and 2081–2100 as the near-term, mid-term and long-term projection, respectively. The multi-model ensemble mean (MME hereinafter) and uncertainty are calculated by the average and standard deviation of the 9-year running-averaged series to remove interannual variability. In addition, the ratio of MME to uncertainty is defined as the signal-to-noise ratio (SNR hereinafter), to represent the significance of the projected change.

### 2.2. *Observational data*

APHRODITE is used to evaluate the CMIP6 models in simulating precipitation over the TP (Yatagai et al., 2012). APHRODITE is a daily and gridded precipitation data based on gauge observations. The horizontal resolution of APHRODITE is 0.5° × 0.5° and the available period is from 1951 to 2015. The observational precipitation data is interpolated conservatively onto 1° × 1° grids.

### 2.3. *Weighting method*

A weighting method is applied to the 27 CMIP6 mod-

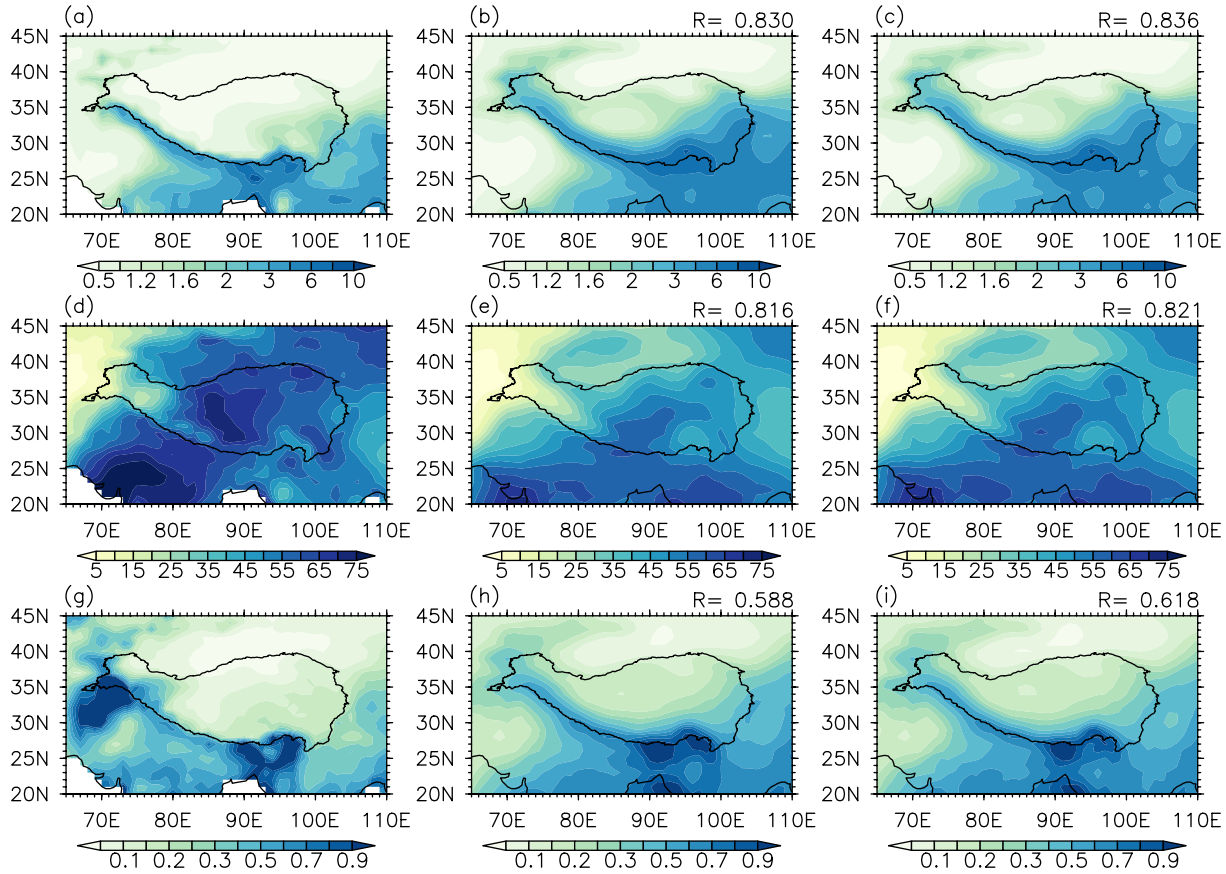


**Fig. 1.** Evaluation of precipitation over the Tibetan Plateau (TP) simulated by the 27 CMIP6 models in terms of equally-weighted multi-model ensemble mean (MME; middle column) and weighted MME (right column) compared to the observation (left column). (a–c) Annual mean precipitation over the TP (mm $d^{-1}$). (d–f) The contribution of summer to the annual total precipitation over the TP (%). (g–i) Interannual variability of annual mean precipitation over the TP (mm $d^{-1}$). *R* values given above panels of the rightmost two columns are pattern correlation coefficient between MME and observation. The TP is outlined by the black curves, where the topography is above 2500 m.

els used as proposed in Sanderson et al. (2017). This method gives each model a different weight according to its quality (skill weight) and independence (uniqueness weight). Here we calculate different weights for models according to their simulation of historical annual or seasonal precipitation within the TP region in terms of the climatology, the contribution of summer (June–July–August mean) to the annual total precipitation, and the interannual variability (i.e. the standard deviation) of precipitation. For each grid within the TP region, the climatology of annual or seasonal precipitation is calculated as:

$$P_{\mathrm{clm}} = \overline{P_{\mathrm{ANN}}}\,, \tag{1}$$

where $P_{\mathrm{ANN}}$ is the annual or seasonal mean precipitation in a specific year and the overbar represents its average value during the historical period (1985–2014). The contribution of summer to the annual total precipitation is calculated as:

$$P_{\mathrm{rate}} = \overline{\frac{P_{\mathrm{JJA}}}{P_{\mathrm{ANN}}}}\,, \tag{2}$$

where $P_{\mathrm{JJA}}$ is the summer precipitation in a specific year. The interannual variability (i.e. the standard deviation) of annual or seasonal precipitation is calculated as:

$$P_{\mathrm{var}} = \sqrt{\frac{1}{N-1}\sum_{i=1}^{N}(P_{\mathrm{ANN}(i)} - P_{\mathrm{clm}})^2}\,, \tag{3}$$

where $i$ indicates years from 1985 to 2014 and $N$ represents the number of years, which is equal to 30 in this study.

The steps to derive the final weights are as follows:

(1) Calculate the area-weighted RMSE between two models (or between model and observation) and normalize it with its mean value;

(2) The distance matrix for metric $v$ is the normalized RMSE $\delta_v$;

(3) The final distance matrix among models (observation) is the linear combination of $\delta_v$:

$$\delta = \sum_{v} \delta_v\,. \tag{4}$$

Considering that the precipitation over the TP shows a remarkable seasonal cycle, it is more important for models

**Table 1**. Institutions, model acronyms, horizontal resolutions for atmospheric components (lat × lon grid points) and final weights of the 27 GCMs analyzed. The bold are 12 models with SSP1-1.9 provided.

| | Institution | Model Acronym | lat × lon grid points | Final Weight |
|---|---|---|---|---|
| 1 | Commonwealth Scientific and Industrial Research Organisation (Australia) | ACCESS-CM2 | 144 × 192 | 0.037 |
| 2 | | ACCESS-ESM1-5 | 145 × 192 | 0.033 |
| 3 | Beijing Climate Center (China) | BCC-CSM2-MR | 160 × 320 | 0.036 |
| 4 | Chinese Academy of Meteorological Sciences (China) | **CAMS-CSM1-0** | 160 × 320 | 0.038 |
| 5 | Canadian Centre for Climate Modelling and Analysis (Canada) | **CanESM5** | 64 × 128 | 0.035 |
| 6 | | CanESM5-CanOE | | 0.033 |
| 7 | National Center for Atmospheric Research, Climate and Global Dynamics Laboratory (USA) | CESM2-WACCM | 192 × 288 | 0.037 |
| 8 | Centre National de Recherches Meteorologiques, Centre Europeen de Recherche et de | CNRM-CM6-1 | 128 × 256 | 0.040 |
| 9 | Formation Avancee en Calcul Scientifique (France) | **CNRM-ESM2-1** | | 0.043 |
| 10 | EC-Earth-Consortium | **EC-Earth3** | 256 × 512 | 0.062 |
| 11 | | **EC-Earth3-Veg** | | 0.062 |
| 12 | Chinese Academy of Sciences (China) | FGOALS-f3-L | 180 × 288 | 0.034 |
| 13 | | **FGOALS-g3** | 80 × 180 | 0.031 |
| 14 | National Oceanic and Atmospheric Administration, Geophysical Fluid Dynamics Laboratory (USA) | GFDL-ESM4 | 180 × 288 | 0.043 |
| 15 | Goddard Institute for Space Studies (USA) | **GISS-E2-1-G** | 90 × 144 | 0.005 |
| 16 | Institute for Numerical Mathematics, Russian Academy of Science (Russia) | INM-CM4-8 | 120 × 180 | 0.027 |
| 17 | | INM-CM5-0 | | 0.026 |
| 18 | Institut Pierre Simon Laplace (France) | **IPSL-CM6A-LR** | 143 × 144 | 0.041 |
| 19 | Department of Geosciences, University of Arizona (USA) | MCM-UA-1-0 | 80 × 96 | 0.009 |
| 20 | MIROC (Japan) | **MIROC6** | 128 × 256 | 0.034 |
| 21 | | **MIROC-ES2L** | 64 × 128 | 0.042 |
| 22 | Max Planck Institute for Meteorology (Germany) | MPI-ESM1-2-HR | 192 × 384 | 0.041 |
| 23 | | MPI-ESM1-2-LR | 96 × 192 | 0.037 |
| 24 | Meteorological Research Institute (Japan) | **MRI-ESM2-0** | 160 × 320 | 0.043 |
| 25 | NCC (Norway) | NorESM2-LM | 96 × 144 | 0.043 |
| 26 | | NorESM2-MM | 192 × 288 | 0.045 |
| 27 | Met Office Hadley Centre (UK) | **UKESM1-0-LL** | 144 × 192 | 0.043 |

to have a good match with observations in terms of the precipitation in wet seasons than in dry seasons. For this purpose, we give metrics related to summer (like the climatology and interannual variability of summer precipitation) the weights of 1.5, and decrease the weights of metrics related to winter (like the climatology and interannual variability of winter precipitation) to 0.5 in the process of linear combination. This is different from Sanderson et al. (2017), where equal weights of metrics were used to get the linear combination of $\delta_v$.

(4) The skill weight for model $i$ is:

$$w_s(i) = e^{-\left(\frac{\delta_{i(obs)}}{Ds}\right)^2}, \quad (5)$$

where $\delta_{i(obs)}$ is the final distance matrix between model $i$ and the observations.

(5) The uniqueness weight for model $i$ is:

$$w_u(i) = \left(1 + \sum_{j \neq i}^{n} e^{-\left(\frac{\delta_{ij}}{Du}\right)^2}\right)^{-1}, \quad (6)$$

where $\delta_{ij}$ is the final distance matrix between models $i$ and $j$. $D_s$ and $D_u$ are skill and uniqueness parameters, respectively. As demonstrated in Sanderson et al. (2015b, 2017), $D_s$ and $D_u$ determine the degree or strength of weighting. Smaller (larger) $D_s$ ($D_u$) results in larger impact of weighting. Note these two parameters only affect the weights of models, while the rank of models in terms of their performance or independence totally depends on their distance matrix (Brunner et al., 2020). Here we use the upper 25% of the distribution of $\delta_{i(obs)}$ (0.7–1.9) in increasing order and the lower 25% of the distribution of $\delta_{ij}$ (0.2–2.0) in increasing order as the values of $D_s(0.9)$ and $D_u(1.1)$, respectively. The sensitivity of results to the values of $D_s$ and $D_u$ is discussed in section 4.

Due to the exponential form of the function (5), the skill weight $w_s$ is restricted between 0 and 1. When $\delta_{i(obs)}$ is close to 0, $w_s$ goes to 1. Conversely, $w_s$ goes toward 0 as $\delta_{i(obs)}$ increases. In terms of the uniqueness weight $w_u$, a model independent of others tends to have a uniqueness weight of 1 as $\delta_{ij}$ is large enough. On the contrary, uniqueness weights for models with similar components decreases with reducing $\delta_{ij}$.

(6) The final weight for model $i$ is:

$$w(i) = Aw_s(i)w_u(i)\,, \tag{7}$$

where $A$ is a unified constant to make $\sum_1^n w(i) = 1$.

### 2.4. *Sensitivity of the projected precipitation to global warming*

The sensitivity of the change in the TP precipitation to global warming is represented by the linear regression coefficient between the global-mean surface air temperature (GSAT) and the projected annual mean precipitation over the TP under each scenario (Zhou et al., 2020). In addition, to analyze the impact of different warming thresholds on the TP precipitation, the relative change in the TP precipitation at the time when increase in GSAT exceeds 1.5°C, 2.0°C, 3.0°C and 4.0°C (relative to 1850–1900) is calculated. The exceedance time is defined as the first year when the 21-year averaged GSAT exceeds the given threshold. Then the relative change in TP precipitation is calculated as the 21-year average around the exceedance year.

## 3. Results

### 3.1. *Evaluation and weights for CMIP6 models*

The evaluation of the precipitation over the TP simulated by the 27 CMIP6 models in terms of MME are shown in Fig. 1. Results show that the precipitation over the TP decreases from the southeastern TP to the northwestern TP. The MME of 27 models can reproduce the spatial pattern of the observed annual mean precipitation over the TP but with a well-recognized wet bias (e.g., Su et al., 2013). Summer (June to August) precipitation contributes more than 50% to the total annual precipitation over the TP in the observations, except for the western TP. In particular, summer precipitation over the central TP (around 87°E) exceeds 70% of the annual total precipitation. The MME of models can reproduce the spatial pattern but underestimates the contribution of summer precipitation to the annual total precipitation over the TP. The observed interannual variability of TP precipitation is larger over the southeastern and the southwestern TP than that over the northern TP. The MME fails to capture the large interannual variability over the southwestern TP and overestimates the variability over other regions of the TP.

To give the weighted projection of the TP precipitation, we first calculate the distance matrix and weights of each model based on the methods introduced in section 2.3. As shown in Fig. 2a, in terms of the RMSE-based matrix, models have better skill in simulating the climatology and interannual variability of the TP precipitation than the contribution of summer to the annual total precipitation.

After scaling by the skill parameter $D_s$, the skill weights of 14 models are larger than the originally average weight (0.037). Especially, EC-Earth3 and EC-Earth3-Veg obtain the highest weights due to their higher agreement with the observations. It is worth noting that the skill weights of GISS-E2-1-G and MCM-UA-1-0 have been decreased for a different reason. To be specific, for GISS-E2-1-G, the weight is limited by its skill in simulating spring and autumn precipitation over the TP, implying the deficiency of the model in simulating TP precipitation in atmospheric circulation transition seasons. By contrast, MCM-UA-1-0 suffers from deficiencies in simulating winter precipitation over the TP for both climatology and interannual variability, indicating bias associated with simulation of snow.

As shown in Fig. 2b, models from the same institute are close to each other, like CanESM5 and CanESM5-OE, CNRM-CM6-1 and CNRM-ESM2-1, EC-Earth3 and EC-Earth3-Veg, INM-CM4-8 and INM-CM5-0. Models from different institutes but sharing similar components of models can also be identified through the distance matrix (Fig. 2b). CAMS-CSM1-0 is found to be close to the MPI models because their atmospheric models are developed based on the same set of model physics and numerics (Müller et al., 2018; Rong et al., 2018). The same is true for NorESM2-MM and CESM2-WACCM as they have same numeric sets for their atmosphere, sea ice and land ice models (Gettelman et al., 2019; Seland et al., 2020). Furthermore, ACCESS-CM2 is close to UKESM1-0-LL because they share the same atmosphere model and similar sea ice models (please see Senior et al., 2020; and https://research.csiro.au/access/what/cm2/). GISS-E2-1-G and MCM-UA-1-0 are distinct from other models and therefore have relatively larger uniqueness weights.

The final unified weights of models are shown in parentheses along $Y$ axis of Fig. 2b, which were used to weight the projections of TP precipitation. As shown in Fig. 1, the simulation of TP precipitation has been improved after weighting. For instance, the pattern correlation coefficients between weighted MMEs and observations increase in terms of all metrics compared to original equally-weighted MMEs. Also the overestimation of the climatology and interannual variability of annual precipitation over the TP has been reduced after weighting, while the underestimation of the contribution of summer to annual precipitation is improved.

### 3.2. *Future change in TP precipitation in weighted CMIP6 projections*

As shown in Table 2, for near-term (2021–40), because of the weak influence of external forcing, the SNRs for near-term projection are less than 100% for SSP2-4.5, SSP3-7.0 and SSP5-8.5, which means the projection uncertainty is large for this period, although weighting reduces the standard deviation slightly. For mid-term (2041–60), with the growing influence of external forcing, the forced responses and SNRs are larger than those for near-term with SNRs all exceeding 100%. For long-term (2081–2100), the change in the TP precipitation is dominated by the external forcing, and the relative increase enhances with the radiation forcing in SSPs. The largest increase in TP precipitation is 21.6% (21.1%) under SSP5-8.5 in terms of weighted (equally-weighted) MME. All SNRs exceed 160% for long-

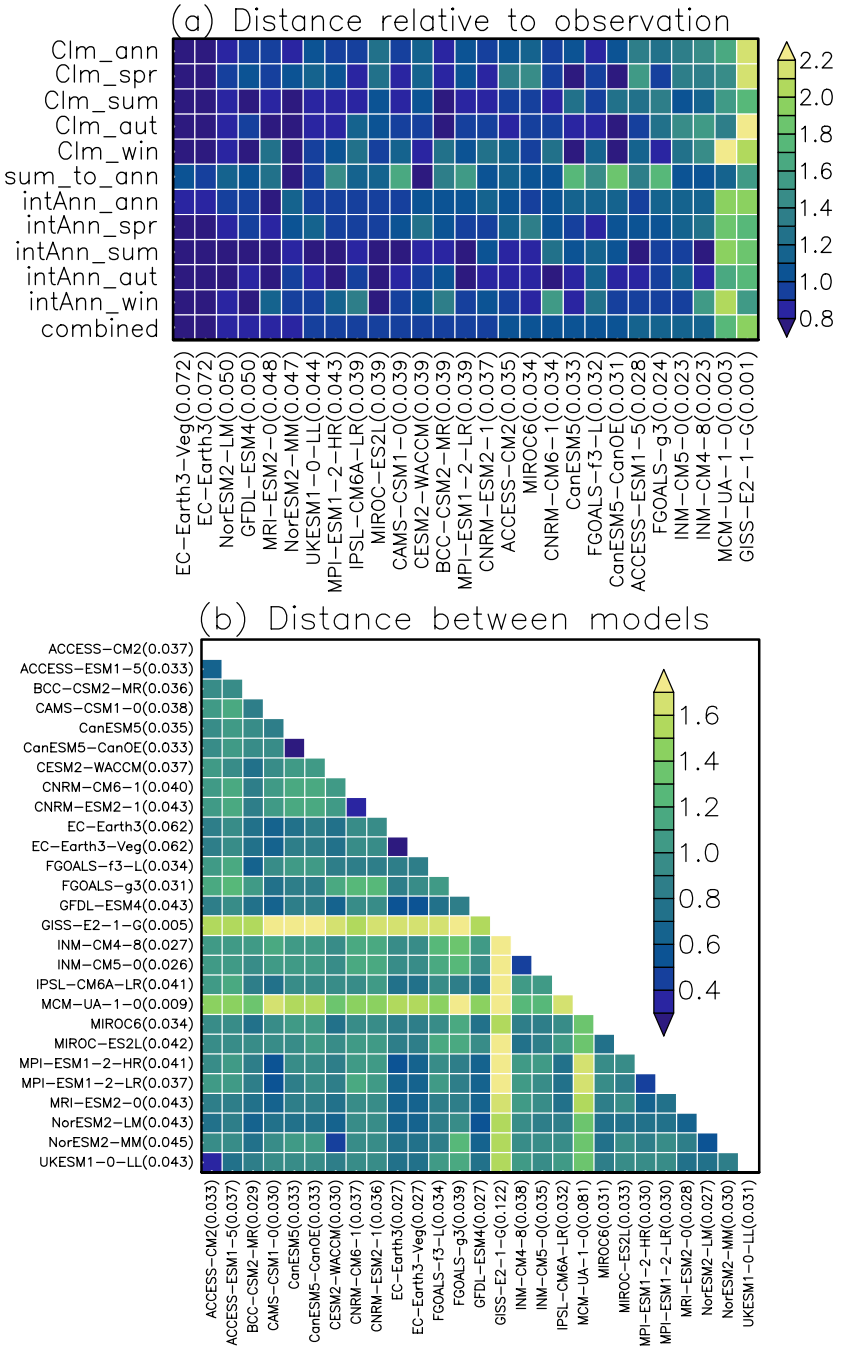


**Fig. 2.** Distance matrix and weights. (a) Distance matrix between models (each column, sorted by unified skill weights in parentheses) and the observation in terms of climatology of annual mean, spring (March to May), summer (June to August), autumn (September to November) and winter (December to February) precipitation, the contribution of summer to the annual total precipitation , interannual variability of annual mean, spring, summer, autumn and winter precipitation, as well as their combined average (each row from top to bottom). (b) Distance matrix in terms of combined metrics between models, with unified uniqueness weights in parentheses along the *x*-axis and unified final weights in parentheses of the *y*-axis.

term projection, indicating the significance of the change in TP precipitation at the end of the century.

Compared to the original equally-weighted projections, the model weighting technique leads to a slightly stronger increase of TP precipitation in the future (Table 2). The larger precipitation change signal leads to larger SNRs in the weighted projections, which are also partly contributed by the slightly reduced uncertainty range. For example, the

**Table 2**. The relative change in TP precipitation (%) relative to 1985–2014 for different future periods and SSPs. Values in the parentheses are standard deviations among models, and values to the right of the parentheses are SNRs.

| | | SSP1-1.9 | SSP1-2.6 | SSP2-4.5 | SSP3-7.0 | SSP5-8.5 |
|---|---|---|---|---|---|---|
| near-term | equally-weighted | 4.9(3.0)164.7 | 3.8(3.0)126.1 | 2.6(3.3)77.6 | 2.8(3.6)77.3 | 3.2(3.9)80.2 |
| | weighted | 5.2(2.9)180.8 | 3.6(2.8)129.4 | 2.5(3.1)79.9 | 2.6(3.4)77.3 | 3.0(3.8)78.8 |
| mid-term | equally-weighted | 6.7(4.0)165.4 | 6.5(4.1)158.0 | 6.3(5.0)126.9 | 5.9(5.6)106.4 | 8.0(6.0)134.6 |
| | weighted | 7.3(3.8)192.9 | 6.6(4.1)161.6 | 6.2(4.8)129.4 | 5.9(5.4)109.2 | 8.0(5.9)136.5 |
| long-term | equally-weighted | 6.9(3.7)186.4 | 8.1(4.9)163.7 | 10.0(5.9)169.4 | 14.7(9.1)162.3 | 21.1(11.1)190.4 |
| | weighted | 7.4(3.5)211.3 | 8.2(4.8)168.9 | 10.2(5.9)173.0 | 15.0(8.8)170.2 | 21.6(10.9)198.8 |

SNR increases from 190.4% to 198.8% (from 162.3% to 170.2%) under SSP5-8.5 (SSP3-7.0) for projections of 2081–2100; meanwhile, the likely (66%) uncertainty range among models decreases slightly from 11.1% to 10.9% (from 9.1% to 8.8%) after weighting. The greater SNRs suggest more robust projections resulted from the weighting method.

The spatial characteristics of the relative change in TP precipitation for long-term projection, as well as the difference between the weighted MME and equally-weighted MME are shown in Figs. 3–8. As shown in Fig. 3, the annual mean precipitation is projected to increase over the whole TP under all SSPs except for SSP1-1.9. Under SSP1-1.9, a decrease by 5% of the annual precipitation is projected but with low agreements among models. The model agreements are also low at the northern and southeastern TP under SSP1-1.9. Under SSP1-2.6 and SSP2-4.5, more than two thirds of the models agree with the increase in the precipitation over the whole TP except for some areas in southwestern TP. With the enhanced external forcing under SSP3-7.0 and SSP5-8.5, the projected increase in the TP precipitation intensifies and shows a good agreement among models. The relative change is stronger over the central and northern TP with an increase over 30% (Figs. 3a–e). Weighting enhances the increase in the precipitation over northwestern Indian Peninsula and northwestern TP, while weakening the increase over the region from the northeastern Indian Peninsula to southern and eastern TP under SSP1-1.9 and SSP1-2.6. For the other three SSPs, differences between weighted and equally-weighted MMEs increase with the growing radiation forcing. The range of enhanced increase in precipitation expands over the TP, and the opposite differences over the northern Indian Peninsula change turns into a prevailing weakened change projected by weighted MME. This implies a stronger increase in precipitation over the TP and a weaker increase over the northern Indian Peninsula can be considered in comparison to the original projection by equally-weighted MME (Figs. 3f–j). In addition, the impact of weighting is pronounced over the basin north of the TP, corresponding to the remarkable change in precipitation relative to present climatology there. Although the models have high consistency in terms of the sign of the change under scenarios with strong radiation forcing, the projected change in TP precipitation shows a range among models.

Spatial patterns of the standard deviation among models in the long-term projection of annual mean precipitation over the TP under SSP5-8.5 are shown in Fig. 4. The standard deviation of model projections is greater than 25% over the northern and the southeastern TP, as well as their adjacent areas like Tarim Basin and the Indian Peninsula. After weighting the models, the range of projections has been reduced over most region of TP, especially for areas with large deviation.

Similar to annual mean precipitation, the change in spring precipitation shows a prevailing increase over the TP projected by weighted MME, and the increase enhances with the growing external forcing (Figs. 5a–e). The location of maximum increase is more eastward for spring relative to annual mean precipitation. In addition, models show a lower consistency in terms of the sign of the projected change in spring precipitation compared to annual mean precipitation. The projection is more consistent among models over the main body of the TP, but with large deviation along the southwestern edges of the TP. For instance, less than two thirds of the models agree with the sign of the change along the southwestern edges even under SSP5-8.5 (Fig. 5e). Weighting enhances the increase in spring precipitation over the central and northern TP and weakens it over the southwestern, southeastern and northeastern TP (Figs. 5f–j). The range of enhanced increase expands and the difference gets more obvious with the growing radiation forcing. The difference of the projected precipitation over the northern Indian Peninsula between weighted and equally-weighted MMEs shows spatial inconsistency under SSP1-1.9 but consistent enhancement under other scenarios.

Different from the annual and spring precipitation, the projected increase in the summer precipitation shows a higher consistency among models over the central and southern TP, which may relate to the consistently strengthened South Asia Summer Monsoon (SASM; Figs. 6a–e). The projected summer precipitation increases over the main body of the TP, with the maximum increase over the southeastern TP. The summer precipitation over the northeastern TP is projected to decrease slightly but the agreement of models is low there. Note the summer precipitation is projected to decrease over regions northwest of the TP, where the precipitation is minimum in summer in terms of climatology and shows a drying trend of summer precipitation in future projections (Jiang et al., 2020; Li et al., 2022). The spatial characteristics of difference in projected summer precipitation

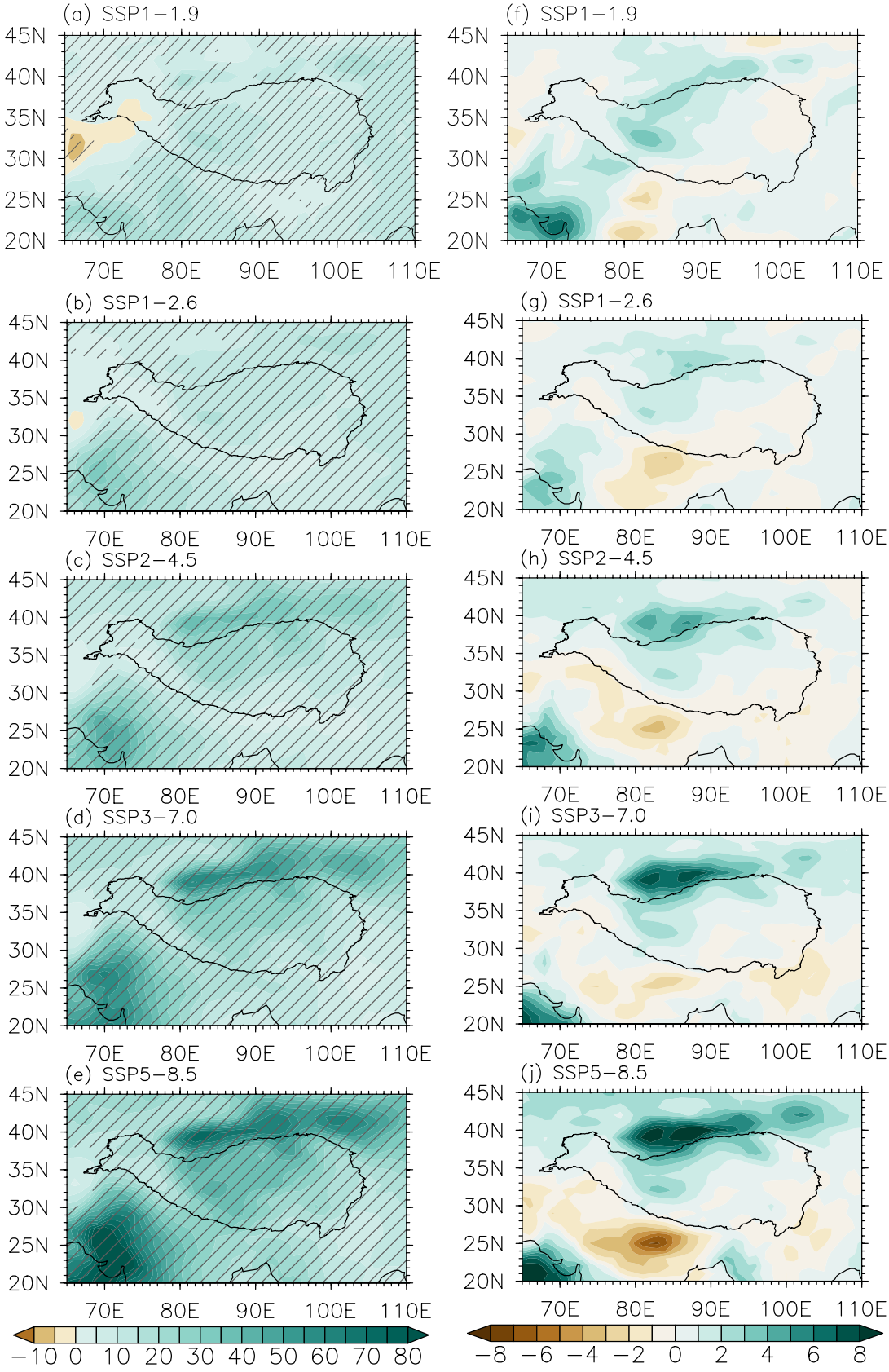


**Fig. 3.** Change in the annual mean precipitation for long-term projection relative to 1985–2014 under (a) SSP1-1.9, (b) SSP1-2.6, (c) SSP2-4.5, (d) SSP3-7.0 and (e) SSP5-8.5 in %. Slashes mean more than two thirds of the models agree with the sign. (f–j) the same as (a–e), but for the difference between weighted and equally-weighted MME.

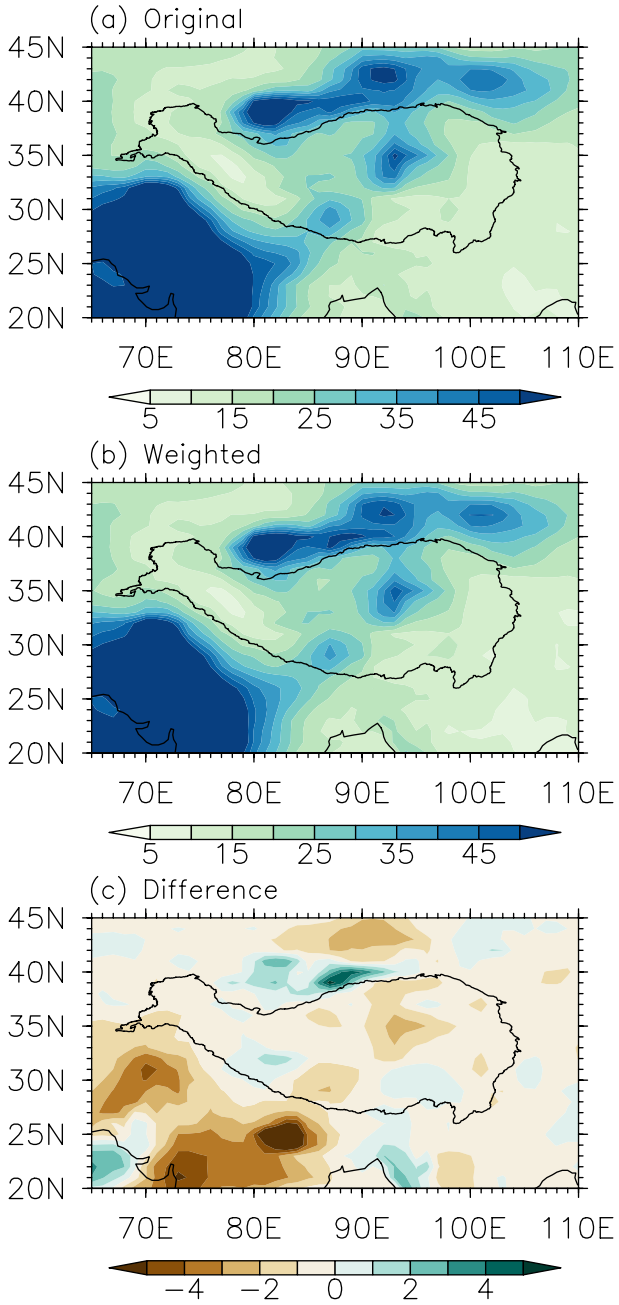


**Fig. 4.** Spatial patterns of the standard deviation among models in the long-term projection of annual mean precipitation over the TP (%) relative to historical period (1985–2014) under SSP5-8.5: (a) equally-weighted MME, (b) weighted MME, (c) difference between weighted and equally-weighted MMEs.

between weighted and equally-weighted MMEs are similar to the case of annual mean precipitation (Figs. 6f–j). The region of enhanced increase is confined within the western and the northwestern TP. The southeastern TP is another region of enhanced increase but the difference is less than that over the northwestern TP. The increasing precipitation over the central to eastern TP is weakened by weighted MME. The inverse impacts of weighting over the northwestern and the northeastern Indian Peninsula under SSP1-1.9 change into a consistent weakened increase over the northern Indian Peninsula under other scenarios. This implies the intensity of the strengthened SASM projected by the original equally-weighted MME is overestimated.

The autumn precipitation over the western part of the TP shows a drying trend under SSP1-1.9 and SSP1-2.6. Other than that, the autumn precipitation is projected to increase with the intensifying external forcing over the entire TP. Models have a high level of agreement in terms of the sign of the change except for the western and the southeastern TP. Generally, the projected autumn precipitation over the TP shows similar spatial patterns to the change in annual mean precipitation (Figs. 7a–e). Resembling the annual and summer precipitation, the influence of weighting on the projected autumn precipitation is more remarkable over the northwestern TP with an intensified increase. The autumn precipitation over the northeastern (northwestern) India Peninsula is weakened (enhanced) after weighting (Figs. 7f–j).

Changes in the winter precipitation over the TP are quite different from changes in other seasons. The winter precipitation shows a moistening trend over the central to northern TP, which intensifies with the growing radiation forcing. In contrast, the winter precipitation is projected to decrease along the southern edges of the TP. Models have a higher consistency regarding the moistening trend than the drying trend (Figs. 8a–e). The difference between weighted and original equally-weighted MMEs in terms of the projected winter precipitation over the TP varies with scenarios, featured by the weakened (enhanced) wetting (drying) trend over the western (southern) TP on the whole (Figs. 8f–j).

### 3.3. *The response of TP precipitation to global warming*

The projected change in the TP precipitation is significantly correlated with the change in the global mean surface temperature (Fig. 9). As shown in Fig. 10 and Table 3, models with high weights are inclined to show higher sensitivity of the projected TP precipitation to the global temperature change. As a result, the mean response of TP precipitation to the increased global surface air temperature among models is enhanced after weighting, especially under SSP1-1.9 (from 8.5% $K^{-1}$ to 9.4% $K^{-1}$) and SSP1-2.6 (from 9.4% $K^{-1}$ to 9.8% $K^{-1}$). In addition, the sensitivity of the TP precipitation to the global temperature change among models is more uncertain under SSP1-1.9 and SSP1-2.6 due to their relatively weak external forcing.

In terms of global warming targets, for scenarios with unanimous GSAT change relative to 1850–1900 above 1.5°C (SSP2-4.5, SSP3-7.0 and SSP5-8.5), the weighted MME change in the TP precipitation is on average about 3.0% relative to present climatology. When unanimous global warming exceeds 2.0°C (for SSP3-7.0 and SSP5-8.5), the averaged TP precipitation increase is about 5.0% in weighted MME. Regarding the 27 models we used, the global warming is extremely unlikely to cross thresholds of 3.0°C or 4.0°C at the end of the century under scenarios

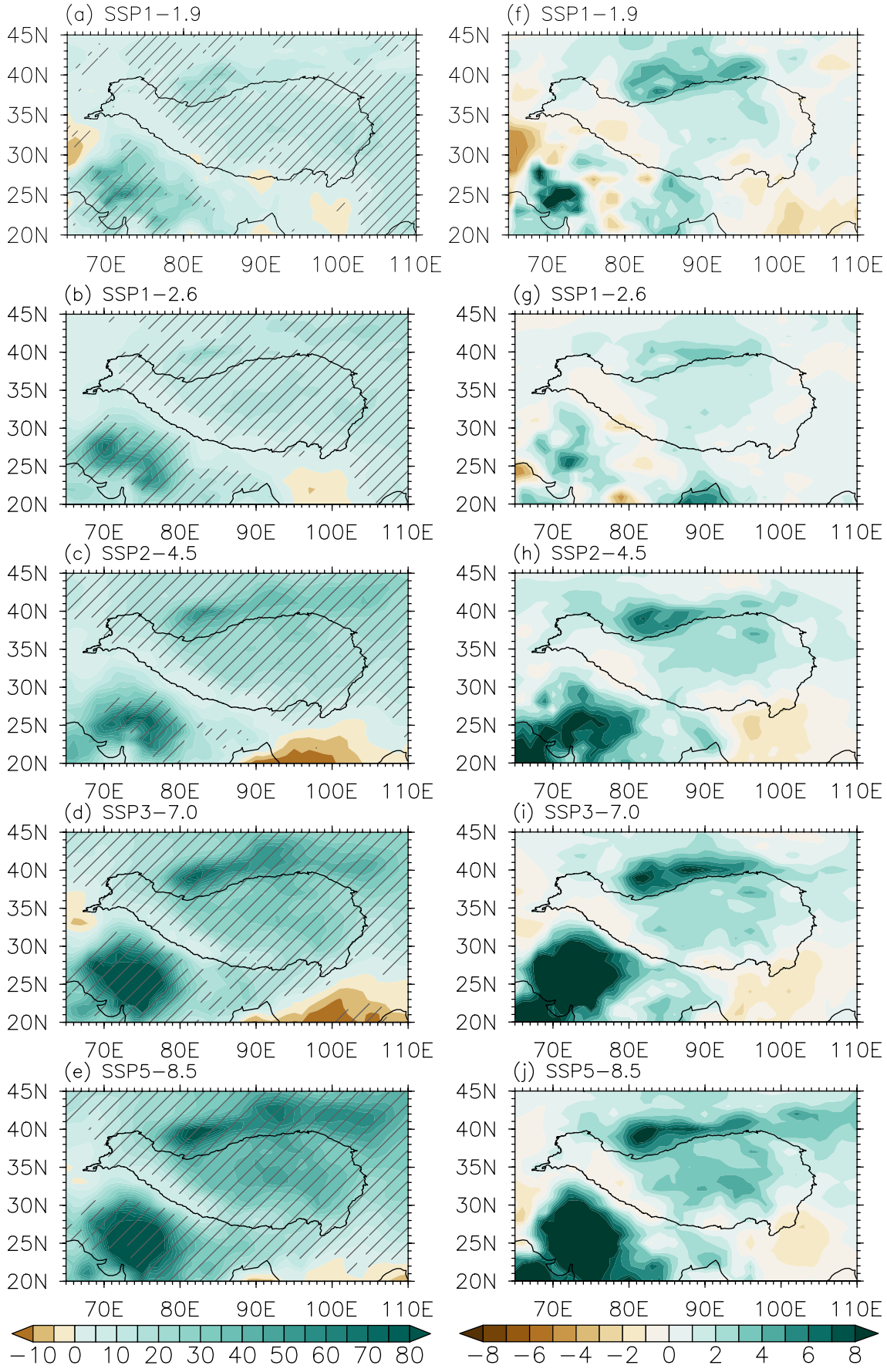


**Fig. 5.** The same as Fig. 3, but for spring precipitation (March–April–May mean).

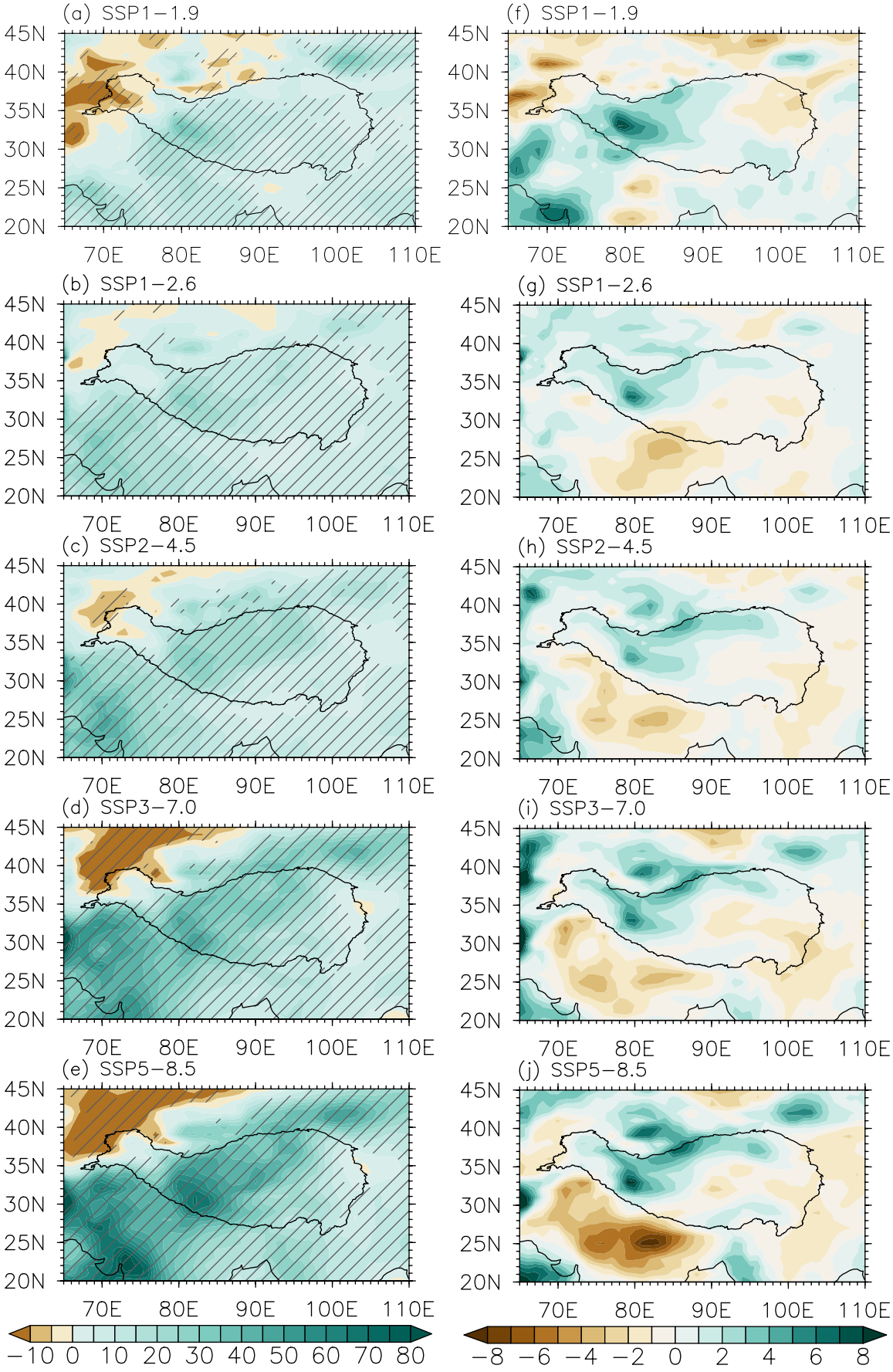


**Fig. 6.** The same as Fig. 3, but for summer precipitation (June–July–August mean).

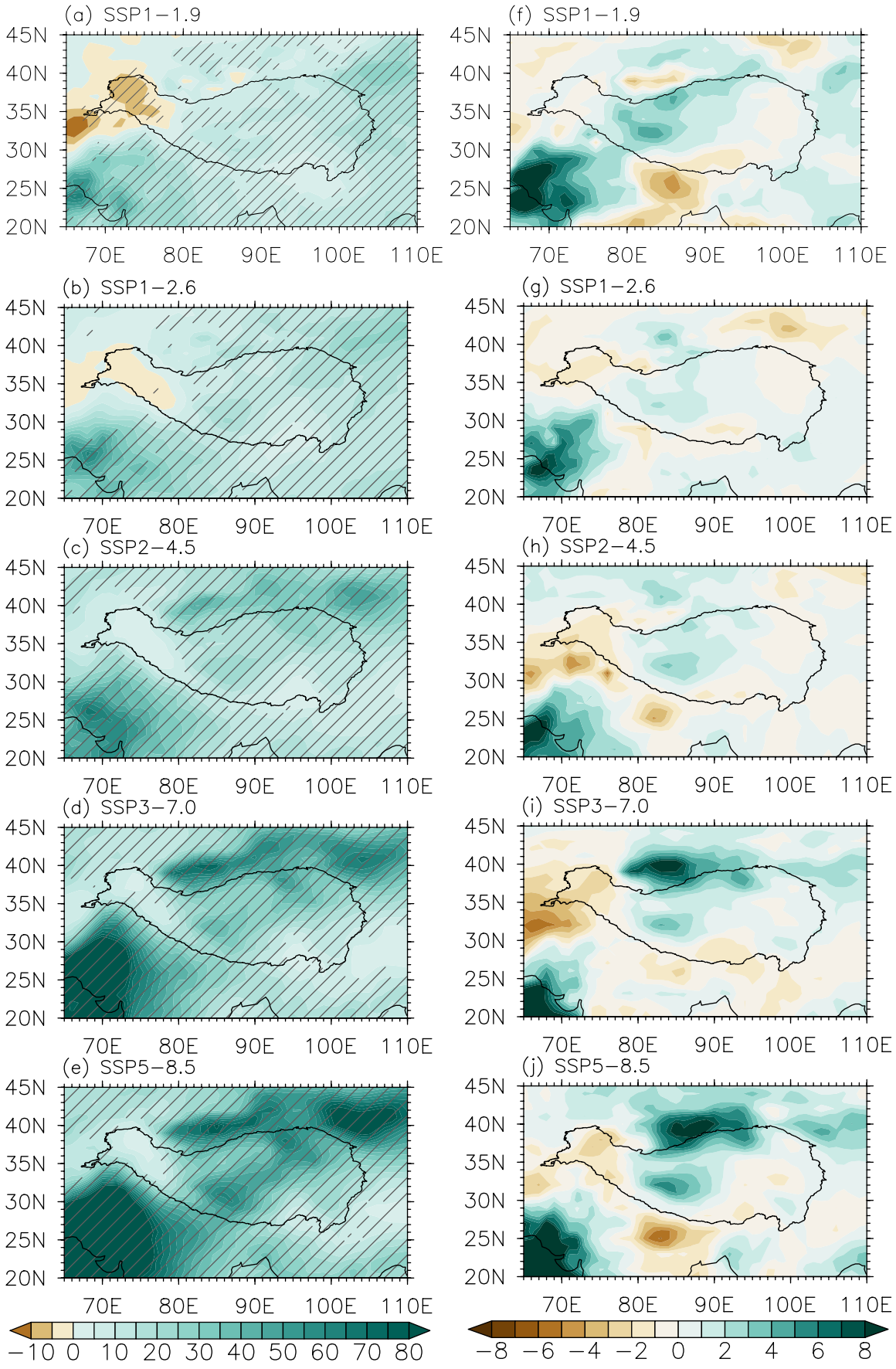


**Fig. 7.** The same as Fig. 3, but for autumn precipitation (September–October–November mean).

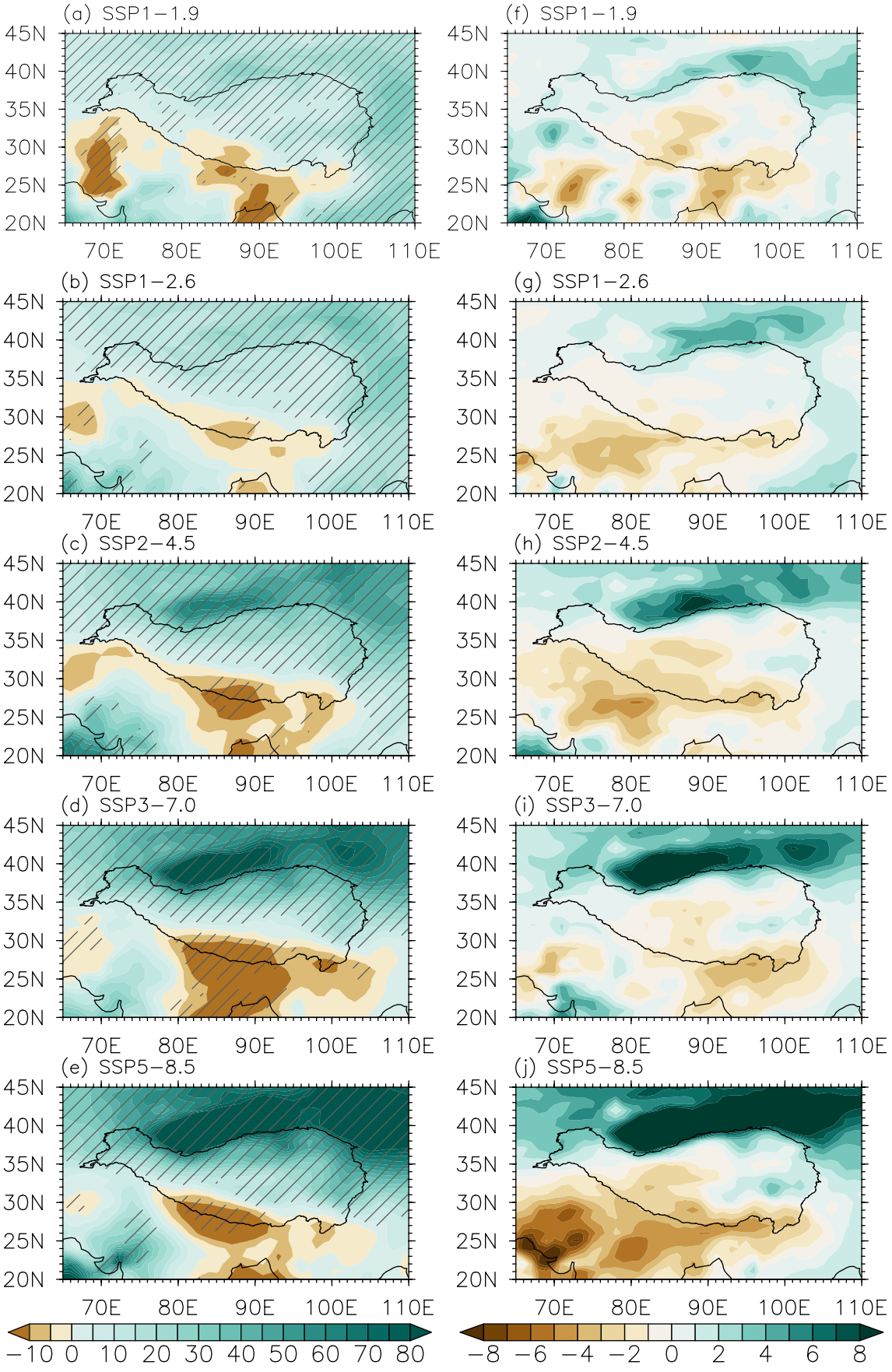


**Fig. 8.** The same as Fig. 3, but for winter precipitation (December–January–February mean).

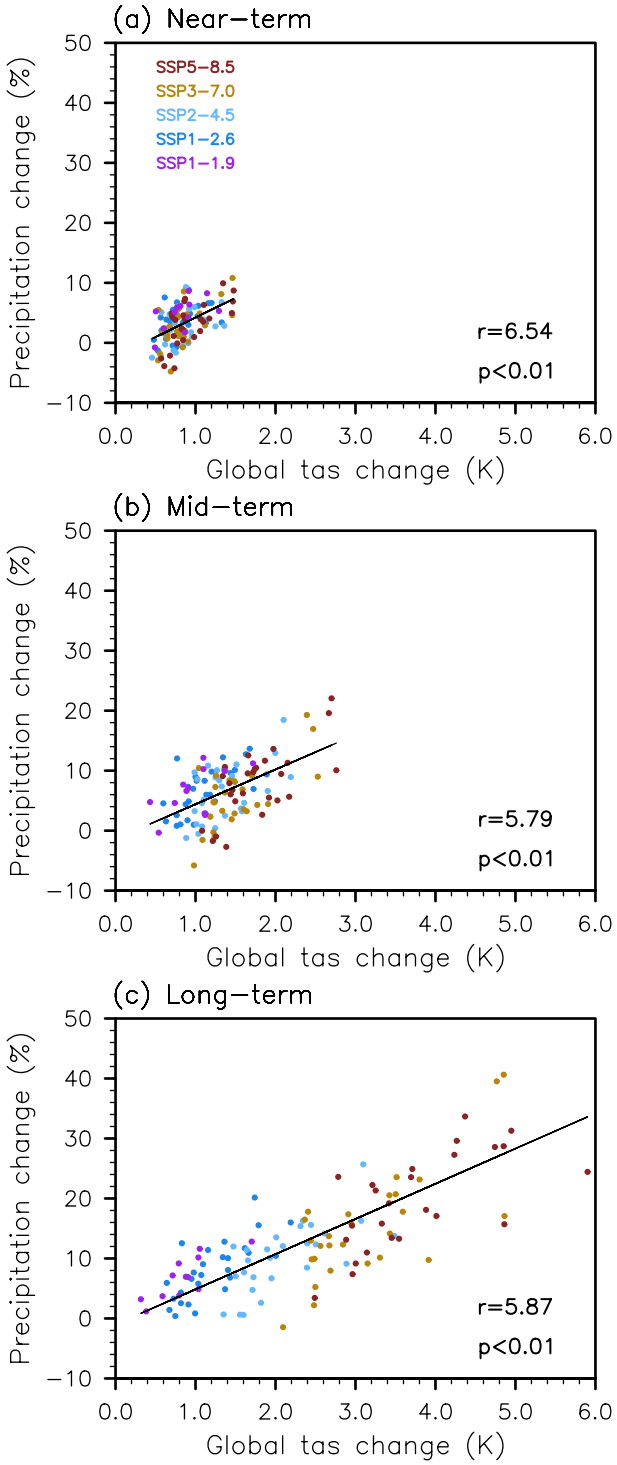


**Fig. 9.** The scatter plots of the change in the global mean surface temperature (units: K) and TP precipitation (units: %) in the (a) near-term (2021–40), (b) mid-term (2041–60), (c) long-term (2081–2100) projection. Dots indicate different models and black lines are linear regression lines, with regression values indicated by $r$ (% K$^{-1}$).

with low emissions, like SSP1-1.9 and SSP1-2.6. Under SSP1-1.9, the relative increase in the TP precipitation is 5.4% and 6.1% when GSAT increase exceeds 1.5°C and 2.0°C, respectively. For SSP1-2.6, the TP precipitation

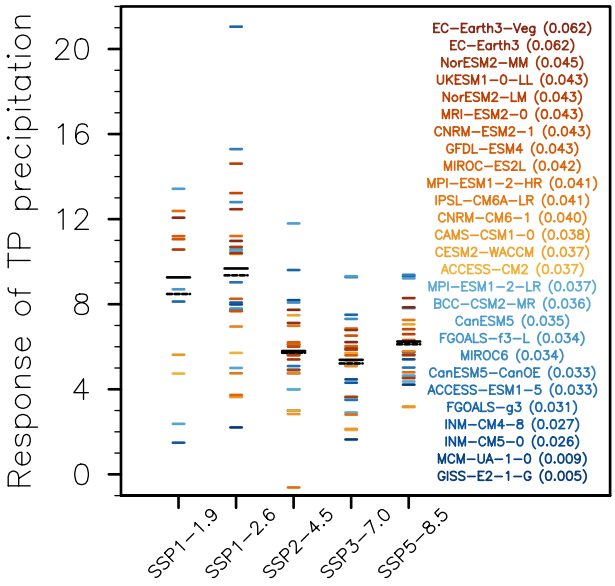


**Fig. 10.** The response of the annual mean precipitation over the TP to the global-mean surface air temperature increase under five scenarios (% K$^{-1}$). Models are sorted according to the weights in the parentheses. The black solid (dashed) lines are weighted (original) MMEs.

increases by 3.6% and 6.8% when GSAT increase exceeds 1.5°C and 2.0°C, respectively (Table 3).

## 4. Summary and discussion

The future change in the precipitation over the TP under global warming is important to the local and downstream ecosystems. Based on a weighting method considering model skill and independence, changes in the TP precipitation under SSP1-1.9, SSP1-2.6, SSP2-4.5, SSP3-7.0 and SSP5-8.5 scenarios are projected by 27 CMIP6 models, as well as its response to global warming targets. The main results are summarized as follows.

(1) The annual mean precipitation is projected to increase over the whole TP with a greater change in the north by the end of 21st century relative to the present climatology. The area-averaged annual mean precipitation over the TP will increase by 7.4%–21.6% by the end of the century under five SSPs projected by the weighted MME. The increase in the annual mean precipitation intensifies with growing external forcing and models agree well with the sign of the change. Except for the drying trend in winter precipitation along the southern edges of the TP, changes in the TP precipitation at seasonal scales show a prevailing moistening trend similar to that of annual mean precipitation.

(2) The model weighting technique generally suggests a slightly stronger increase in TP precipitation in the future but with spatial and seasonal differences in details. The enhanced increase shows the highest spatial consistency in terms of the change in spring precipitation over the TP. Regarding annual, summer and autumn precipitation, the influence of weighting is more remarkable over the northwest-

**Table 3**. The sensitivity of the TP precipitation to the global warming (% $K^{-1}$), and responses of the TP precipitation to different thresholds of the global warming (%). In terms of different thresholds, values in the parentheses are standard deviations among models, and values right to the parentheses are the percentage of models whose exceedances are true.

| | | SSP1-1.9 | SSP1-2.6 | SSP2-4.5 | SSP3-7.0 | SSP5-8.5 |
|---|---|---|---|---|---|---|
| Sensitivity | equally-weighted | 8.5 | 9.4 | 5.7 | 5.2 | 6.1 |
| | weighted | 9.3 | 9.7 | 5.8 | 5.4 | 6.2 |
| 1.5 °C | equally-weighted | 5.1(2.6)67 | 3.9(2.4)81 | 3.2(3.2)100 | 2.9(3.3)100 | 3.2(3.3)100 |
| | weighted | 5.4(2.6) | 3.6(2.1) | 3.0(3.0) | 2.8(3.2) | 3.1(3.3) |
| 2.0 °C | equally-weighted | 6.0(1.7)33 | 6.9(2.8)44 | 5.6(4.1)96 | 4.7(3.4)100 | 5.3(3.8)100 |
| | weighted | 6.1(1.5) | 6.8(2.8) | 5.4(3.9) | 4.6(3.3) | 5.3(3.8) |
| 3.0 °C | equally-weighted | –(–)0 | –(–)0 | 11.7(3.3)30 | 9.6(3.9)85 | 11.5(4.1)96 |
| | weighted | –(–)0 | –(–)0 | 11.5(2.9) | 9.6(3.9) | 11.6(4.2) |
| 4.0 °C | equally-weighted | –(–)0 | –(–)0 | 22.5(4.0)7 | 17.8(5.4)37 | 18.6(4.9)56 |
| | weighted | –(–)0 | –(–)0 | 22.5(2.8) | 17.9(4.8) | 19.1(4.8) |

ern TP, which gives us more confidence in a wetter northwestern TP in the future. Weighting also reduces the model uncertainty in projecting TP precipitation regarding both the areal average and regional changes, especially at regions with large standard deviations among models.

(3) With the United Nations Sustainable Development Goals and the Paris Agreement, global-scale efforts are underway to limit global warming levels, such as the 2°C or 1.5°C warming targets relative to preindustrial levels (UNFCCC, 2015). In particular, SSP1-1.9 and SSP1-2.6 are designed to achieve stabilized global warming of 1.5°C and 2°C, respectively. Based on the weighted projections, for SSP1-1.9 (SSP1-2.6), the relative increase in the annual mean TP precipitation is 5.4% (3.6%) and 6.1% (6.8%) when GSAT increase exceeds 1.5°C and 2.0°C, respectively.

Although the values of parameters $D_s$ and $D_u$ do not affect the rank of models, they have influence on the final weights, as well as the effect of weighting. From this perspective, the sensitivity of the difference between weighted and original results to variant values of $D_s$ and $D_u$ is tested and shown in Fig. 11. Results show the effect of weighting is more sensitive to $D_s$ than to $D_u$. As shown in Fig. 11a, ratios of weighted to original results in terms of the relative change in TP precipitation, standard deviation among models and the SNR are around 1.0 despite different values of $D_u$. This implies the effect of weighting is not very sensitive to the values of $D_u$, which may relate to the close distance between models. In contrast, values of $D_s$ have larger influence on the effect of weighting due to the relatively far distance between the observation and simulations. As shown in Fig. 11b, the relative change in TP precipitation increases with reducing $D_s$, especially for values less than 0.9, resulting from the decreased model variation and increased SNR. To conclude, it is qualitatively consistent that model weighting leads to slight increases in precipitation change and SNR, and decreases in model deviation, although quantitative projections are slightly affected by weighting parameters. In addition, it is worth noting that limited observations over the TP, especially its western part,

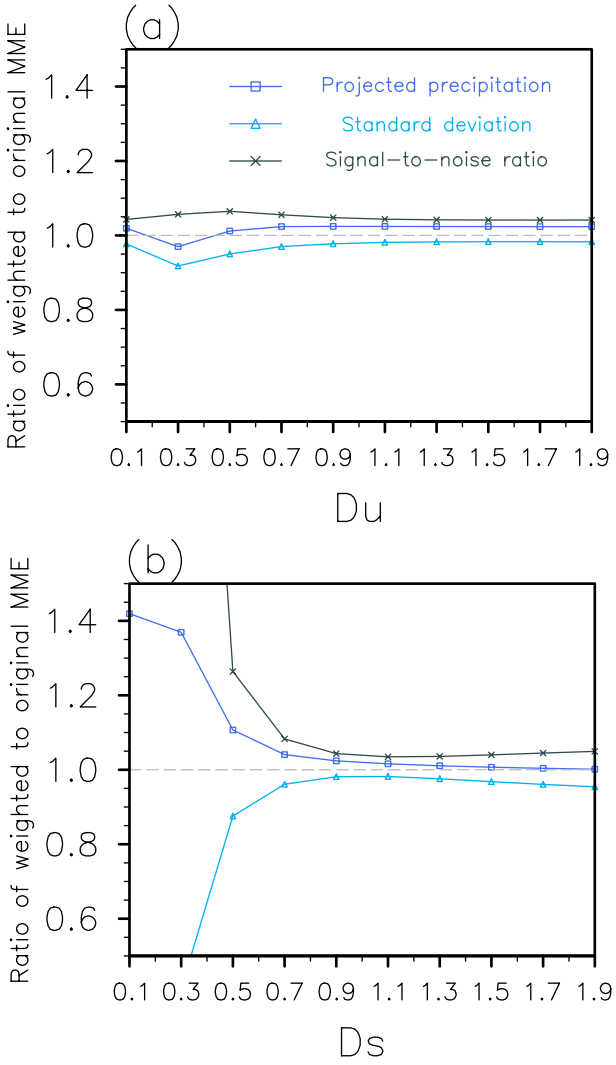


**Fig. 11.** Ratios of weighted MME to equally-weighted MME for long-term projections under SSP5-8.5 varying with different values of $D_u$ or $D_s$. (a) The case of $D_s$ = 0.9. (b) The case of $D_u$ = 1.1. The blue, skyblue and green lines represent relative change in the annual mean TP precipitation, standard deviation among models and the signal-to-noise ratio, respectively.

may lead to uncertainties in evaluating the model performances.

In order to produce more reliable future projections, different methods have been proposed including weighting models according to their independence and performance, emergent constraints and decadal predictions initialized by observations. However, no consensus has been reached on a robust and universal method to get the optimal projections (Lee et al., 2021). The model weighting method used in this study focuses on model performance in simulating historical climate, which is the necessary condition for a reasonable future projection, as well as model independence to get a balance between the size and validness of samples. Results concerning the increasing precipitation over the TP in the future is consistent with previous studies (Su et al., 2013; Fu et al., 2021; Xie and Wang, 2021; Yang et al., 2021). Furthermore, difference between weighted and equally-weighted MMEs can give us more confidence on the future climate of the TP from specific aspects, such as the stronger increase in the precipitation over the TP, especially for the season of spring and the region of the northwestern TP.

***Acknowledgements***. This work is supported by the Strategic Priority Research Program of the Chinese Academy of Sciences under Grant No. XDA20060102, the Second Tibetan Plateau Scientific Expedition and Research (STEP) program (Grant No 2019QZKK0102), the National Natural Science Foundation of China under Grant No. 41988101 and K. C. WONG Education Foundation. The observational precipitation data APHRODITE can be obtained from http://aphrodite.st.hirosaki-u.ac.jp/download/. The model data from CMIP6 can be found at https://esgf-node.llnl.gov/search/cmip6/. Considerable gratitude is owed to the corresponding working teams.



## REFERENCES

Amos, M., and Coauthors, 2020: Projecting ozone hole recovery using an ensemble of chemistry–climate models weighted by model performance and independence. *Atmospheric Chemistry and Physics*, **20**(16), 9961–9977, https://doi.org/10.5194/acp-20-9961-2020.

Brunner, L., R. Lorenz, M. Zumwald, and R. Knutti, 2019: Quantifying uncertainty in European climate projections using combined performance-independence weighting. *Environmental Research Letters*, **14**(12), 124010, https://doi.org/10.1088/1748-9326/ab492f.

Brunner, L., A. G. Pendergrass, F. Lehner, A. L. Merrifield, R. Lorenz, and R. Knutti, 2020: Reduced global warming from cmip6 projections when weighting models by performance and independence. *Earth System Dynamics*, **11**(4), 995–1012, https://doi.org/10.5194/esd-11-995-2020.

Duan, A. M., R. Z. Sun, and J. H. He, 2017: Impact of surface sensible heating over the Tibetan Plateau on the western Pacific subtropical high: A land–air–sea interaction perspective. *Adv. Atmos. Sci.*, **34**(2), 157–168, https://doi.org/10.1007/s00376-016-6008-z.

Eyring, V., S. Bony, G. A. Meehl, C. A. Senior, B. Stevens, R. J. Stouffer, and K. E. Taylor, 2016: Overview of the Coupled Model Intercomparison Project Phase 6 (CMIP6) experimental design and organization. *Geoscientific Model Development*, **9**(5), 1937–1958, https://doi.org/10.5194/gmd-9-1937-2016.

Feng, L., and T. J. Zhou, 2017: Projection of summer precipitation change over the Qinghai-Tibetan Plateau with a 20 km high-resolution global climate model. *Plateau Meteorology*, **36**(3), 587–595. (in Chinese with English abstract)

Fu, Y. H., X. J. Gao, Y. M. Zhu, and D. Guo, 2021: Climate change projection over the Tibetan Plateau based on a set of RCM simulations. *Advances in Climate Change Research*, **12**, 313–321, https://doi.org/10.1016/j.accre.2021.01.004.

Gao, Y. H., L. H. Xiao, D. L. Chen, J. W. Xu, and H. W. Zhang, 2018: Comparison between past and future extreme precipitations simulated by global and regional climate models over the Tibetan Plateau. *International Journal of Climatology*, **38**(3), 1285–1297, https://doi.org/10.1002/joc.5243.

Gettelman, A., and Coauthors, 2019: The whole atmosphere community climate model version 6 (WACCM6). *J. Geophys. Res.: Atmos.*, **124**(23), 12 380–12 403, https://doi.org/10.1029/2019JD030943.

Hao, Z. C., Q. Ju, W. J. Jiang, and C. J. Zhu, 2013: Characteristics and scenarios projection of climate change on the Tibetan Plateau. *The Scientific World Journal*, **2013**, 129793, https://doi.org/10.1155/2013/129793.

Hu, Q., D. B. Jiang, and G. Z. Fan, 2015: Climate change projection on the Tibetan Plateau: Results of CMIP5 models. *Chinese Journal of Atmospheric Sciences*, **39**(2), 260–270, https://doi.org/10.3878/j.issn.1006-9895.1406.13325. (in Chinese with English abstract)

Immerzeel, W. W., and M. F. P. Bierkens, 2012: Asia's water balance. *Nature Geoscience*, **5**(12), 841–842, https://doi.org/10.1038/ngeo1643.

Immerzeel, W. W., L. P. H. Van Beek, and M. F. P. Bierkens, 2010: Climate change will affect the Asian water towers. *Science*, **328**(5984), 1382–1385, https://doi.org/10.1126/science.1183188.

Immerzeel, W. W., and Coauthors, 2020: Importance and vulnerability of the world's water towers. *Nature*, **577**(7790), 364–369, https://doi.org/10.1038/s41586-019-1822-y.

Ji, Z. M., and S. C. Kang, 2013: Double-nested dynamical downscaling experiments over the Tibetan Plateau and their projection of climate change under two RCP scenarios. *J. Atmos. Sci.*, **70**(4), 1278–1290, https://doi.org/10.1175/JAS-D-12-0155.1.

Jiang, J., T. J. Zhou, X. L. Chen, and L. X. Zhang, 2020: Future changes in precipitation over Central Asia based on CMIP6 projections. *Environmental Research Letters*, **15**, 054009,

https://doi.org/10.1088/1748-9326/ab7d03.

Knutti, R., J. Sedláček, B. M. Sanderson, R. Lorenz, E. M. Fischer, and V. Eyring, 2017: A climate model projection weighting scheme accounting for performance and interdependence. *Geophys. Res. Lett.*, **44**(4), 1909–1918, https://doi.org/10.1002/2016GL072012.

Lee, J.-Y., and Coauthors, 2021: Future global climate: Scenario-based projections and near-term information. *Climate Change 2021: The Physical Science Basis. Contribution of Working Group I to the Sixth Assessment Report of the Intergovernmental Panel on Climate Change*, V. Masson-Delmotte et al., Eds., Cambridge University Press.

Li, L. L., J. Li, and R. C. Yu, 2022: Evaluation of CMIP6 HighResMIP models in simulating precipitation over Central Asia. *Advances in Climate Change Research*, **13**(1), 1–13, https://doi.org/10.1016/j.accre.2021.09.009.

Li, T., Z. H. Jiang, L. L. Zhao, and L. Li, 2021: Multi-model ensemble projection of precipitation changes over China under global warming of 1.5 and 2°C with consideration of model performance and independence. *J. Meteor. Res.*, **35**(1), 184–197, https://doi.org/10.1007/s13351-021-0067-5.

Liang, Y. X., N. P. Gillett, and A. H. Monahan, 2020: Climate model projections of 21st century global warming constrained using the observed warming trend. *Geophys. Res. Lett.*, **47**(12), e2019GL086757, https://doi.org/10.1029/2019GL086757.

Liu, S. F., A. M. Duan, and G. X. Wu, 2020: Asymmetrical response of the East Asian summer monsoon to the quadrennial oscillation of global sea surface temperature associated with the Tibetan Plateau thermal feedback. *J. Geophys. Res.: Atmos.*, **125**(20), e2019JD032129, https://doi.org/10.1029/2019JD032129.

Lorenz, R., N. Herger, J. Sedláček, V. Eyring, E. M. Fischer, and R. Knutti, 2018: Prospects and caveats of weighting climate models for summer maximum temperature projections over North America. *J. Geophys. Res.: Atmos.*, **123**(9), 4509–4526, https://doi.org/10.1029/2017JD027992.

Merrifield, A. L., L. Brunner, R. Lorenz, I. Medhaug, and R. Knutti, 2020: An investigation of weighting schemes suitable for incorporating large ensembles into multi-model ensembles. *Earth System Dynamics*, **11**(3), 807–834, https://doi.org/10.5194/esd-11-807-2020.

Müller, W. A., and Coauthors, 2018: A higher-resolution version of the Max Planck Institute Earth System Model (MPI-ESM1.2-HR). *Journal of Advances in Modeling Earth Systems*, **10**(7), 1383–1413, https://doi.org/10.1029/2017MS001217.

O'Neill, B. C., and Coauthors, 2016: The Scenario Model Intercomparison Project (ScenarioMIP) for CMIP6,. *Geoscientific Model Development*, **9**(9), 3461–3482, https://doi.org/10.5194/gmd-9-3461-2016.

Pritchard, H. D., 2019: Asia's shrinking glaciers protect large populations from drought stress. *Nature*, **569**(7758), 649–654, https://doi.org/10.1038/s41586-019-1240-1.

Riahi, K., and Coauthors, 2017: The shared socioeconomic pathways and their energy, land use, and greenhouse gas emissions implications: An overview. *Global Environmental Change*, **42**, 153–168, https://doi.org/10.1016/j.gloenvcha.2016.05.009.

Rong, X. Y., and Coauthors, 2018: The CAMS climate system model and a basic evaluation of its climatology and climate variability simulation. *J. Meteor. Res.*, **32**(6), 839–861, https://doi.org/10.1007/s13351-018-8058-x.

Sanderson, B. M., R. Knutti, and P. Caldwell, 2015a: Addressing interdependency in a multimodel ensemble by interpolation of model properties. *J. Climate*, **28**(13), 5150–5170, https://doi.org/10.1175/JCLI-D-14-00361.1.

Sanderson, B. M., R. Knutti, and P. Caldwell, 2015b: A representative democracy to reduce interdependency in a multimodel ensemble. *J. Climate*, **28**(13), 5171–5194, https://doi.org/10.1175/JCLI-D-14-00362.1.

Sanderson, B. M., M. Wehner, and R. Knutti, 2017: Skill and independence weighting for multi-model assessments. *Geoscientific Model Development*, **10**(6), 2379–2395, https://doi.org/10.5194/gmd-10-2379-2017.

Seland, Ø., and Coauthors, 2020: Overview of the Norwegian Earth System Model (NorESM2) and key climate response of CMIP6 DECK, historical, and scenario simulations. *Geoscientific Model Development*, **13**(12), 6165–6200, https://doi.org/10.5194/gmd-13-6165-2020.

Senior, C. A., and Coauthors, 2020: U.K. community Earth system modeling for CMIP6,. *Journal of Advances in Modeling Earth Systems*, **12**(9), e2019MS002004, https://doi.org/10.1029/2019MS002004.

Su, F. G., X. L. Duan, D. L. Chen, Z. C. Hao, and L. Cuo, 2013: Evaluation of the global climate models in the CMIP5 over the Tibetan Plateau. *J. Climate*, **26**(10), 3187–3208, https://doi.org/10.1175/JCLI-D-12-00321.1.

United Nations Framework Convention on Climate Change (UNFCCC), 2015: Decision 1/CP.21. The Paris Agreement. 32 pp. Available online at http://unfccc.int/resource/docs/2015/cop21/eng/l09r01.pdf. Accessed on 13 December 2019.

Wang, X. J., G. J. Pang, and M. X. Yang, 2018: Precipitation over the Tibetan Plateau during recent decades: A review based on observations and simulations. *International Journal of Climatology*, **38**(3), 1116–1131, https://doi.org/10.1002/joc.5246.

Xie, Z. L., and B. Wang, 2021: Summer heat sources changes over the Tibetan Plateau in CMIP6 models. *Environmental Research Letters*, **16**(6), 064060, https://doi.org/10.1088/1748-9326/ac0279.

Xu, Y., X. J. Gao, and F. Giorgi, 2010: Upgrades to the reliability ensemble averaging method for producing probabilistic climate-change projections. *Climate Research*, **41**, 61–81, https://doi.org/10.3354/cr00835.

Yang, X. L., B. T. Zhou, Y. Xu, and Z. Y. Han, 2021: CMIP6 evaluation and projection of temperature and precipitation over China. *Adv. Atmos. Sci.*, **38**(5), 817–830, https://doi.org/10.1007/s00376-021-0351-4.

Yao, T. D., and Coauthors, 2012: Different glacier status with atmospheric circulations in Tibetan Plateau and surroundings. *Nature Climate Change*, **2**(9), 663–667, https://doi.org/10.1038/nclimate1580.

Yatagai, A., K. Kamiguchi, O. Arakawa, A. Hamada, N. Yasutomi, and A. Kitoh, 2012: APHRODITE: Constructing a long-term daily gridded precipitation dataset for Asia based on a dense network of rain gauges. *Bull. Amer. Meteor. Soc.*, **93**(9), 1401–1415, https://doi.org/10.1175/BAMS-D-11-00122.1.

Zhang, D. F., and X. J. Gao, 2020: Climate change of the 21st century over China from the ensemble of RegCM4 simulations. *Chinese Science Bulletin*, **65**(23), 2516–2526, https://doi.org/10.1360/TB-2020-0231. (in Chinese with English

abstract)

Zhang, H. W., Y. H. Gao, J. W. Xu, Y. Xu, and Y. S. Jiang, 2019: Decomposition of future moisture flux changes over the Tibetan Plateau projected by global and regional climate models. *J. Climate*, **32**(20), 7037–7053, https://doi.org/10.1175/JCLI-D-19-0200.1.

Zhang, R. H., and Coauthors, 2015: An overview of projected climate and environmental changes across the Tibetan Plateau in the 21st century. *Chinese Science Bulletin*, **60**(32), 3036–3047, https://doi.org/10.1360/N972014-01296. (in Chinese with English abstract)

Zhou, T. J., W. X. Zhang, X. L. Chen, L. X. Zhang, L. W. Zou, and W. M. Man, 2020: The near-term, mid-term and long-term projections of temperature and precipitation changes over the Tibetan Plateau and the sources of uncertainties. *Journal of the Meteorological Sciences*, **40**(5), 697–710, https://doi.org/10.3969/2020jms.0076. (in Chinese with English abstract)